Journal of Alloys and Compounds 886 (2021) 161333

Contents lists available at ScienceDirect

Journal of Alloys and Compounds

journal homepage: www.elsevier.com/locate/jalcom

Effect of manganese on the grain boundary network of lath martensite in precipitation hardenable stainless steels

Vinothkumar Govindaraj[a,b], Ehsan Farabi[a], Sitarama Kada[a], Peter D. Hodgson[a], Rajkumar P Singh[b], Gregory S. Rohrer[c], Hossein Beladi[a,*]

[a] Institute for Frontier Materials, Deakin University, VIC 3216, Australia
[b] Kalyani Center for Technology and Innovation, Bharat Forge, Pune 411036, India
[c] Department of Materials Science and Engineering, Carnegie Mellon University, Pittsburgh, PA 15213-3890, USA

ARTICLE INFO

Article history:
Received 29 April 2021
Received in revised form 22 July 2021
Accepted 24 July 2021
Available online 28 July 2021

Keywords:
Lath martensite
Grain boundary network
17-4 PH
Five-parameter analysis
Phenomenological theory of martensite

ABSTRACT

The fully martensitic microstructures of a manganese bearing precipitation hardenable (PH) stainless steel and a commercial 17-4 PH steel were compared to investigate the influence of chemical composition on the grain boundary network of the lath martensitic microstructure. The martensitic transformation in both steels led to the bimodal misorientation angle distribution having multiple maxima at misorientations in the range of 10–15° and 50–60°. This closely matched with the misorientations between variants associated with the Kurdjumov-Sachs orientation relationship (K-S OR). However, the Mn addition appeared to relatively reduce the area of boundaries with misorientations near 60°. This was a result of the reduction in the area of 60°/[011] intervariant boundaries in the Mn bearing steel. The phenomenological theory of martensite revealed that the Mn addition altered the 3-variant clustering (i.e., $V_1V_3V_5$) in 17-4PH steel to the 4-varaint clustering (i.e., $V_1V_2V_3V_5$) arrangement to minimize the strain associated with the displacive martensitic transformation, promoting the population of 60°/[111] intervariant boundaries at the expense of 60°/[011] intervariant boundary. The changes in local variant selection affected the connectivity of the grain boundary network, suggesting that grain boundary network characteristics (i.e., population and connectivity) of the lath martensite microstructure can be manipulated by altering the chemical composition of the steel. The five-parameter grain boundary analysis for both martensitic steels, however, revealed similar grain boundary plane distributions for all boundaries associated with the K-S OR, being terminated on {011} planes due to the constraint that results from the displacive phase transformation.

1. Introduction

The exceptional combination of high strength, ductility, fatigue and corrosion resistance of precipitation-hardened (PH) martensitic stainless steel has been made it an increasingly important material in the aviation, energy and defence sectors. Due to the low content of carbon in martensitic PH steels, the martensite is relatively soft and strengthening is largely provided by the precipitation of non-carbide phases such as Cu [1–3], Lave phases [1,2], β′-NiAl [4–6] and η-Ni3Ti/Al [7–9]. The most widely used PH martensitic steel is the 17-4 PH grade (Fe-17Cr-4Ni-(3-5)Cu-0.07C), strengthened by precipitation of coherent Cu in the martensitic matrix [3–8]. The chromium in 17-4 PH steel provides the material with exceptional corrosion resistance while the Ni addition expands the austenitic phase region, bringing versatility to the 17-4PH steel [3,4]. Although, the alloy is being widely used for a variety of applications, new approaches can be taken to reduce the amount of the more expensive nickel element in the material. For example, Mn can be regarded as a suitable replacement for Ni [9] as it can expand the austenite phase field and participates in the precipitation process [20]. Therefore, this is an effective way to develop cost-effective Ni-lean PH stainless steels. However, Ni and Mn have different effects on the austenite phase field and martensitic transformation temperature, which significantly influence the martensitic microstructure of PH stainless steels [18].

The martensitic PH steel exhibits a hierarchical lath martensitic microstructure subdividing the parent austenite grain into packets and blocks [23]. A block consists of a set of similarly orientated martensite laths (i.e., martensite variants) whereas the group of variants with distinct orientations sharing the same habit plane

* Corresponding author.
E-mail address: hossein.beladi@deakin.edu.au (H. Beladi).

https://doi.org/10.1016/j.jallcom.2021.161333
0925-8388/

forms a packet. The strength, ductility and toughness of martensitic steels are significantly altered by the block and packet size and their characteristic intervariant boundaries [24–26]. In particular, the intervariant boundary characteristics, which include their crystallographic orientation, population and connectivity (intervariant boundary network), are strongly influenced by the crystallography of the martensite transformation. Apparently, the intersection of variants (variant arrangement/clustering) during the martensitic transformation largely depends on the associated shape strain developed during the shear transformation and the involved accommodation mechanism (i.e., slip and twinning) [23,27–29]. Therefore, the Bain strain is strongly linked with the lattice parameters of the parent and daughter phases, making the strain and selection of variants susceptible to minimal composition variations of the PH steel [22,23,29]. It was shown that the presence of Mn in a martensitic steel promotes specific variant pairing (i.e., local variant selection) to minimize the shape strain [23,24,29,30], where the transformation twinning (rather dislocation slip) is the dominant mechanism to accommodate the strain associated with the martensitic transformation. However, it is not clear yet how the steel composition (e.g., Mn) alters the grain boundary network of PH steels, transformed through a given martensitic phase transformation mechanism (i.e., dislocation slip). This is important as changes in the distribution of grain boundaries can significantly alter diffusion [10–12] and grain growth [13] phenomena, and the mechanical response of steel such as strength [14,15], toughness [16,17] and creep [18]. It can be concluded that the crystallographic orientation relationship between austenite and ferrite, and the occurrence of variant selection (i.e., more frequent appearance of some variants than the others) during the martensite phase transformation should be considered as a major factor in designing novel PH steels.

In the current study, the role of alloying element (i.e., Mn) on the grain boundary network (i.e., plane, population and connectivity) of the lath martensitic microstructure was studied using the five-parameter analysis along with the homology metrics approach. Later, the phenomological theory of martensite was used to describe strain development during the transformation and its role on the intervariant boundary characteristic development in PH martensitic steels. These findings ultimately make it possible to predict the intervariant network formation in martensitic steels and engineer the microstructure with an optimum intervariant boundary network for a specific application.

2. Experimental procedure

The compositions of the precipitation hardenable stainless steels used in the current study are presented in Table 1. Steel B is commercially available, known as 17-4 PH, and Steel A was developed using the ThermoCalc approach, as discussed in [9], to partially replace Ni by Mn. The latter was prepared by air induction melting route and cast under argon atmosphere at SAAR LOHA, India. The ingots were forged at 1200 °C into 150 mm × 30 mm × 30 mm rectangular bars at Bharat Forge, India. Both steels were subjected to a solution-annealing heat treatment, involving reheating to 1035 ± 5 °C and being held isothermally for 60 min followed by air-cooling to room temperature, hereafter called the as-quenched condition. To determine the transformation temperatures, the samples of 4 mm diameter and 10 mm height were tested on a DIL805A/D horizontal loading dilatometer under a vacuum of 10^{-5} mbar and at a heating rate of 10 °C/s. The as-quenched samples were electro-etched in 60% HNO_3 for about 30–45 s at ~45 V at room temperature to distinguish prior austenite grain boundaries. The average prior austenite grain size was measured using the linear intercept method.

For XRD analysis, the samples were mirror-polished using OPS solution after standard metallography preparation. The lattice parameters of the as-quenched martensite was measured from the XRD scans performed using a Panalytical X′pert PRO MRD XL machine equipped with Cu source operating with an applied voltage of 50 kV and current of 40 mA.

The in-situ elevated temperature XRD experiments were conducted to measure the lattice parameter of austenite at different temperatures using Panalytical X′Pert Powder diffractometer equipped with a PIXCEL detector. The in-situ heating was carried out using the flat plate setup in an Anton Paar HTK 1200N with an oven chamber. The samples with a dimension of 10 × 10 × 0.5 mm^3 were placed on a ceramic plate, heated uniformly to 1000 °C at a rate of 10 °C/min. The non-ambient chamber was maintained under a vacuum of ~10^{-5} mbar. After 30 min of holding, the XRD scan was performed in the 2θ range between 40° and 100°, a suitable range to obtain austenite peaks for the lattice parameter calculation. During cooling, the XRD scan was performed at different temperatures between 1000 and 700 °C after 30 min holding at each temperature. Following the standard calibration procedures, the lattice parameter of austenite at each temperature was determined by a Pawley refinement using the TOPAS profile fitting software and the lattice parameter was extrapolated linearly as a function of temperature to determine the lattice parameter of austenite at room temperature (i.e., 25 °C).

Samples for SEM-EBSD analysis were carefully prepared according to the aforementioned standard metallography procedure. The SEM-EBSD characterization of the as-quenched samples was performed on an FEI Quanta 3D FEG FIB-SEM microscope using an OIM™ detector. Each scan was performed at 20 kV voltage and 4 nA current with a step size of 0.15 µm over an area of 5 × 120 × 120 $µm^2$. The post-processing analysis was performed using TSL software. The data were cleaned by a grain dilation routine and then a single average orientation per grain was assigned with a tolerance angle of 5°. The confidence index was ~0.65 on average. The boundaries were reconstructed with a tolerance of 2 times the step size (i.e., the maximum deviation between reconstructed boundary and corresponding boundary segments was 2 times the step size). The number of boundary segments were 59,000 and 63,000 for steels A and B, respectively. An automated stereographic projection approach (known as 'five-parameter analysis' [19]) was employed to measure the grain boundary planes character distribution formed during martensitic transformation in both steels. The homology metrics approach described in detail elsewhere [20] was used to determine the grain boundary network connectivity of the martensitic microstructures.

TEM samples were thinned to 50–60 µm. The 3 mm disc standard TEM slices were punched from the thin samples, which were then electro-polished using a Struers Tenupol-5 Twin-jet electro-polishing machine with 10% perchloric acid, 90% ethanol solution mixed with liquid N_2 at ~−30 °C, and ~15 V. The electro-polished sample was loaded to a double-tilting TEM sample holder. TEM examinations were performed on a FEI Tecnai T20 TEM.

Table 1
Chemical composition of steels used in the current study.

Composition (wt%)	C	Si	Mn	P	S	Cr	Ni	Cu	Nb
Steel A	0.035	0.11	3.31	0.016	0.01	11.95	2.87	2.64	0.16
Steel B	0.043	0.34	0.87	0.022	0.001	15.85	4.7	4.12	0.23

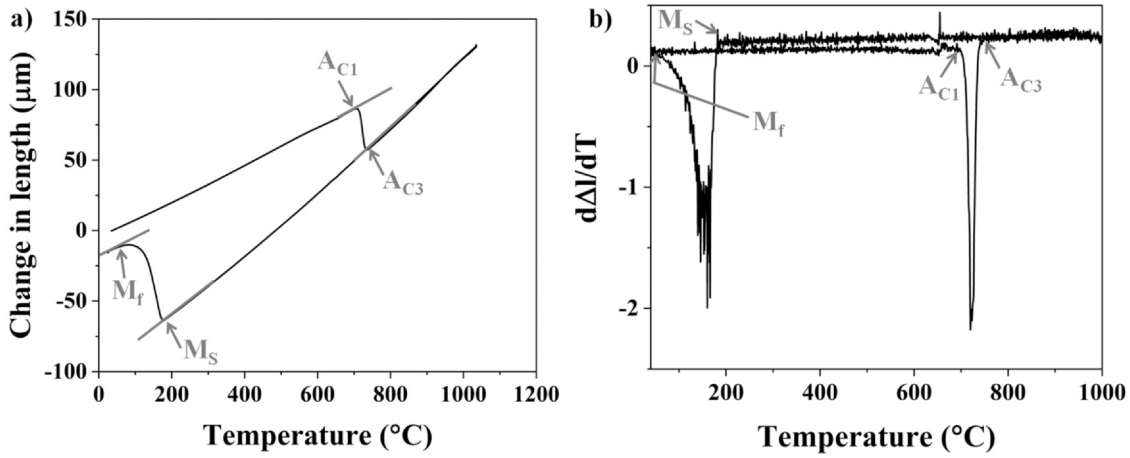

Fig. 1. a) dilatometer result of Steel A, showing the characteristic dilation (i.e., change in length with respect to temperature) features associated with the phase transformations; b) first derivative of dilation against temperature, displaying deflections at the austenite start (A_{C1}) and finish (A_{C3}) transformation temperatures and martensite start (M_S) and finish (M_f) transformation temperatures.

3. Results

The dilatometer result of steel A for heating and cooling rates of 10 °C/s showed characteristic dilation features in the transformation temperature range, indicating the occurrence of only austenite and martensite transformations upon the heating and cooling regimes, respectively (Fig. 1a). For precise determination of critical transformation temperatures, the first derivative of the dilation data was plotted against the temperature and the transformation temperatures were identified from the marked deflections in the plot (Fig. 1b). Accordingly, the critical transformation temperatures of both steels such as austenite start (A_{C1}) and finish (A_{C3}) temperatures, and martensite start (M_s) and finish (M_f) temperatures were determined (Table 2). It should be noted that the employed vacuum cooling method cannot cool the samples below room temperature, casting a certain level of uncertainty on the measured M_f temperature.

The as-quenched microstructure of the steels displayed a parallel stacked martensite lath morphology featuring a high dislocation density (Fig. 2). The measured average prior austenite grain size was around 32 ± 7 µm and 45 ± 7 µm for Steel A and Steel B, respectively. Second phase particles were occasionally observed in the as-quenched microstructures (indicated by the white solid arrow in Fig. 2a), which were identified as MX type niobium carbides (NbC) having an FCC crystal structure after indexing the selected area diffraction (SAD) pattern taken on one of the precipitates along the [011] beam direction (Fig. 2a inset). They were in the size range of 50–150 nm. Because of their small volume fraction, the XRD results obtained from the as-quenched microstructures of both steels showed no sign of NbC precipitates and only the characteristic peaks related to BCC crystal structure such as $110_{\alpha'}$, $200_{\alpha'}$, $211_{\alpha'}$, $220_{\alpha'}$ (Fig. 3), suggesting the complete transformation of austenite to martensite. The absence of an orientation relationship between the matrix and the NbC precipitates indicates that they persisted during solution-annealing heat treatment. In other words, the solution-annealing temperature was not high enough to dissolve all NbC precipitates.

3.1. Grain boundary characterization

During the martensitic transformation, a single austenite grain can theoretically transform to 12 or 24 different orientations (variants), depending on the parent austenite and daughter (martensite) phase orientation relationship. Due to the very low carbon content (i.e., <0.043 wt% C), the orientation relationship was assumed to be the Kurdjumov-Sachs OR in both steel compositions. In other words, a given parent austenite grain potentially transforms to 24 martensitic variants, as listed in Table 3. The intersection of one variant with the other 23 variants results in 23 intervariant boundaries (i.e., angle/axis pairs). However, only 16 independent intervariant boundary misorientations can be observed as some intervariant boundaries are identical due to the cubic symmetry [21]. For example, the intervariant boundary misorientation that forms from the intersection of V1 with V3 (i.e., 60°/[011]) and V1 with V5 (60°/[0-1-1]) are identical due to the cubic symmetry. Based on these distinct lattice misorientations, the block and packet can be identified in the martensitic microstructure, as shown in Fig. 4. Here, the block was delineated by intervariant boundaries resulted from the impingement of two distinct variants belonging to a given family, sharing the same habit plane (e.g., the first six variants; V_1-$V_{i=2-6}$ in Table 3). To determine the packets, the angle/axis pairs that resulted from the intersection of variants belonging to two distinct families with different habit planes were traced (Fig. 4). Based on this classification, the average block size of Steels A and B was measured 5.26 ± 0.53 µm and 4.72 ± 0.35 µm and the packet size was 7.96 ± 0.68 µm and 9.1 ± 0.66 µm, respectively (Table 2).

3.1.1. Misorientation angle distribution

The as-quenched microstructure of both steels qualitatively showed a similar misorientation angle distribution with distinct peaks at ~53° and ~60° (Fig. 5). However, the as-quenched microstructure of Steel B displayed a relatively higher population at ~60°. There was a slight difference in the low angle range (5–20°), but not significant when compared to high angle range. In general, the misorientation angle distribution of both steels largely matched the

Table 2
Critical transformation temperatures of steels A and B at heating and cooling rates of 10 °C/s and their martensitic microstructure characteristics.

Steel	Ac_1 (°C)	Ac_3 (°C)	M_s (°C)	M_f (°C)	d_γ (µm)	Block size (µm)	Packet size (µm)
A	694	749	182	48	32 ± 7	5.26 ± 0.53	7.96 ± 0.68
B	740	860	189	–	45 ± 7	4.72 ± 0.35	9.1 ± 0.66

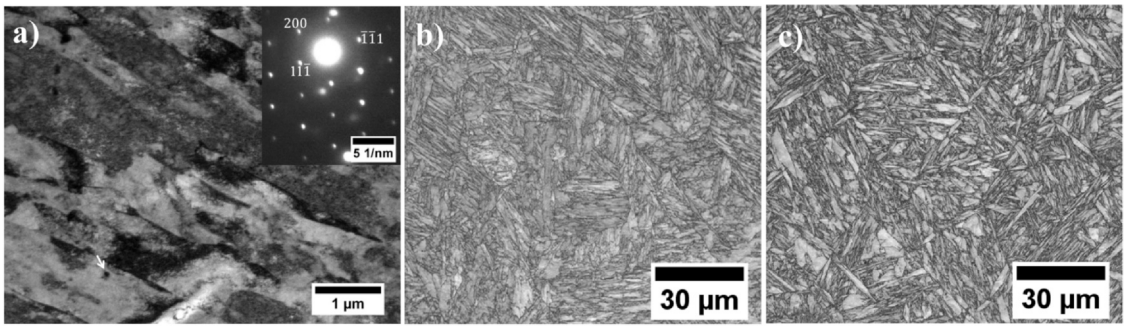

Fig. 2. a) TEM bright field image of as-quenched Steel A, showing the lath martensite microstructure with high dislocation density [9]: SAD pattern taken on a NbC precipitate (indicated by white solid arrow), confirms its FCC crystal structure (inset in "a"). b) and c) EBSD image quality of Steel A and Steel B, respectively.

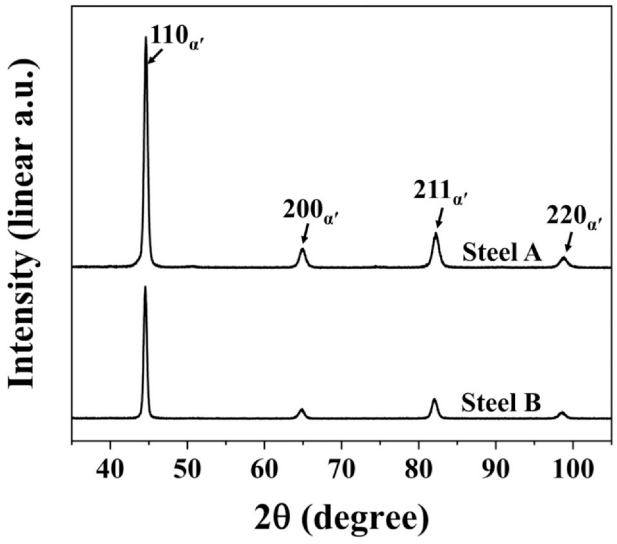

Fig. 3. XRD results of Steels A and B, showing only the characteristic peaks related to BCC crystal structure. α′ represents martensite; a.u. – linear arbitrary unit.

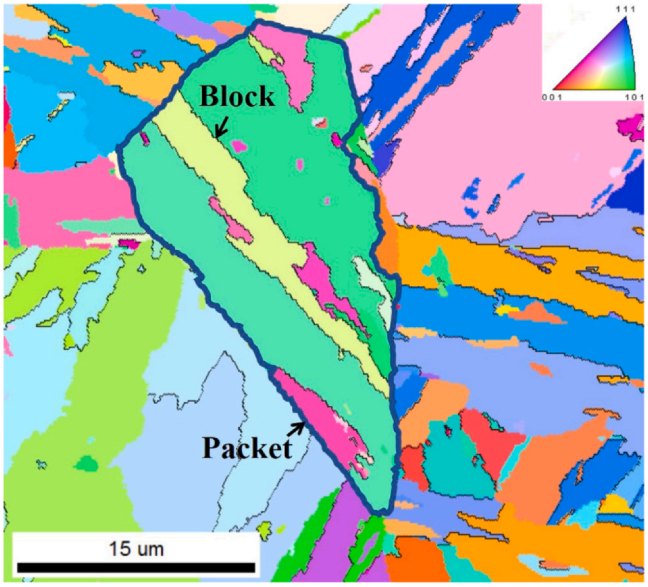

Fig. 4. EBSD map of Steel A, demonstrating the block and packet features in the as-quenched microstructure.Inset is the colour codes referring to normal direction.

Table 3
Intervariant boundaries resulted from the impingement of variants associated with the K-S OR [31].

Variant	Plane parallel	Direction parallel	Rotation angle/axis from V1
V1	$(111)_\gamma$ || $(011)_{\alpha'}$	$[-101]_\gamma$ || $[-1-11]_{\alpha'}$	–
V2		$[-101]_\gamma$ || $[-11-1]_{\alpha'}$	60° / [11-1]
V3		$[1]_\gamma$ || $[-1-11]_{\alpha'}$	60° / [011]
V4		$[1]_\gamma$ || $[-11-1]_{\alpha'}$	10.5° / [0-1-1]
V5		$[1-10]_\gamma$ || $[-1-11]_{\alpha'}$	60° / [0-1-1]
V6		$[1-10]_\gamma$||$[-11-1]_{\alpha'}$	49.5°/ [011]
V7	$(1-11)_\gamma$ || (011)	$[10-1]_\gamma$||$[-1-11]_{\alpha'}$	49.5° / [-1-11]
V8		$[10-1]_\gamma$||$[-11-1]_{\alpha'}$	10.5° / [11-1]
V9		$[-1-10]_\gamma$||$[-1-11]_{\alpha'}$	50.5° / [-10 3 -13]
V10		$[-1-10]_\gamma$ || $[-11-1]_{\alpha'}$	50.5° / [-7 -5 5]
V11		$[011]_\gamma$ || $[-1-11]_{\alpha'}$	14.9° / [13 5 1]
V12		$[011]_\gamma$ || $[-11-1]_{\alpha'}$	57.2° / [-3 5 6]
V13	$(-111)_\gamma$ || $(011)_{\alpha'}$	$[0-11]_\gamma$ || $[-1-11]_{\alpha'}$	14.9° / [5 -13 -1]
V14		$[0-11]_\gamma$ || $[-11-1]_{\alpha'}$	50.5° / [-5 5 -7]
V15		$[-10-1]_\gamma$ || $[-1-11]_{\alpha'}$	57.2° / [-6 -2 5]
V16		$[-10-1]_\gamma$ || $[-11-1]_{\alpha'}$	20.6° / [11 -11 -6]
V17		$[110]_\gamma$ || $[-1-11]_{\alpha'}$	51.7° / [-11 6 -11]
V18		$[110]_\gamma$ || $[-11-1]_{\alpha'}$	47.1° / [-24 -10 21]
V19	$(11-1)_\gamma$	$[-110]_\gamma$ || $[-1-11]_{\alpha'}$	50.5° / [-3 13 10]
V20	|| $(011)_{\alpha'}$	$[-110]_\gamma$ || $[-11-1]_{\alpha'}$	57.2° / [3 6 -5]
V21		$[0-1-1]_\gamma$ || $[-1-11]_{\alpha'}$	20.6° / [30-1]
V22		$[0-1-1]_\gamma$ || $[-11-1]_{\alpha'}$	47.1° / [-10 21 24]
V23		$[101]_\gamma$ || $[-1-11]_{\alpha'}$	57.2° / [-2 -5 -6]
V24		$[101]_\gamma$ || $[-11-1]_{\alpha'}$	21.1° / [9 -4 0]

ones theoretically expected from the intersection of K-S martensite variants, falling in the range of 10–22° and 47–60° (Table 3). The misorientation angle population in the range of 22–46° was relatively low (Fig. 5). This range represented boundaries resulting from the impingement of variants from either side of a given prior austenite grain boundary.

3.1.2. Intervariant boundary population

To assess the intervariant boundaries distribution, the length fractions of intervariant boundaries was measured through tracing the lattice misorientations (i.e., angle/axis) associated with the K-S OR in the martensitic microstructures. The length fractions of intervariant boundaries belonging to the K-S OR showed qualitatively similar distributions, having the dominant 60°/[011] intervariant boundary population (Fig. 6). However, the population of 60°/[011] intervariant boundary was much greater in Steel B (~46%) compared with Steel A (~32%). By contrast, the 60°/[111] boundary (i.e., V1-V2) revealed higher population in Steel A (5.0%) than Steel B (2.3%).

3.1.3. Intervariant boundary plane character distribution

The intervariant boundary plane distribution independent of misorientation was qualitatively similar for both martensitic steels, showing a strong anisotropic distribution towards the (101) position (Fig. 7). The Steel A showed maxima of ~1.9 MRD and minima of ~0.4

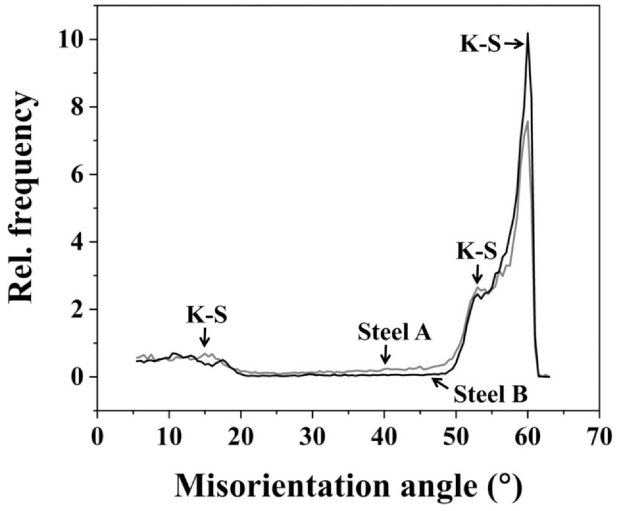

Fig. 5. Misorientation angle distribution of both steels, showing distinct peaks largely associated with the K-S OR.

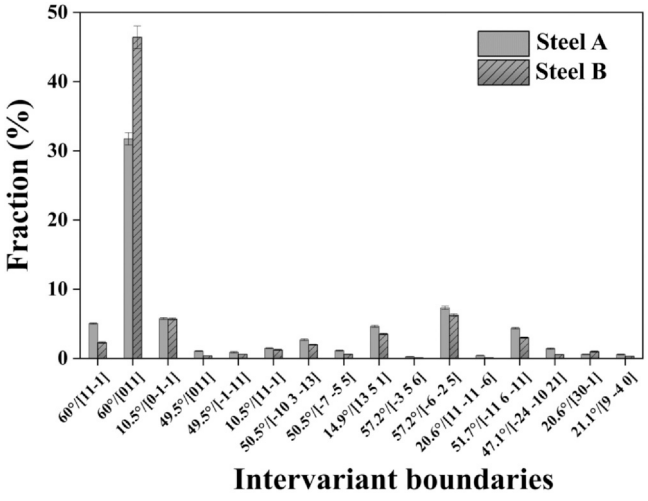

Fig. 6. Distribution of intervariant boundaries of martensitic microstructure in both steels, associated with the K-S OR.

MRD about the (101) and (001) positions, respectively (Fig. 7a). The maxima of ~1.9 MRD at the (101) position implies that the population of (101) was 90% greater than the expected value in a random distribution. In other words, most intervariant boundary interfaces were terminated on {101} planes. Similarly, the distribution of Steel B displayed maxima (~1.8 MRD) at the (101) position and minima (~0.4 MRD) at the (001) position. In addition, the intervariant boundary plane distribution of Steel B revealed a spread towards the (111) position (Fig. 7b).

Figs. 8–9 and A.1 represent the intervariant boundary plane character distribution, calculated for all boundaries associated with the K-S OR. In general, the intervariant boundary plane character distribution varied with lattice misorientation, though the characteristics of the distribution were largely comparable for a given misorientation for both martensitic steels (Figs. 8–9 and A.1). For the intervariant boundaries with a 10.5° misorientation about the [111] axis, maxima are found for mixed boundaries with {110} orientations in both martensitic steels (Fig. 8a and 8d). For a 49.5° misorientation about [111], the maxima are on the zone axis of tilt boundaries (i.e., (1 -6 6)||(1 6 -6), Fig. 8b and 8e) for both martensitic microstructures. The peaks were, indeed, very close to {110}||{110}

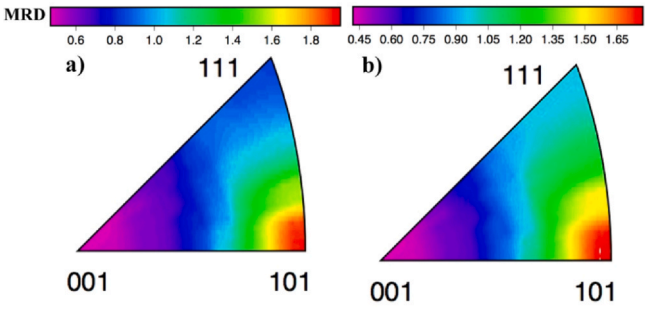

Fig. 7. The distribution of intervariant boundary planes character of lath martensite microstructures of a) Steel A and) Steel B. MRD represents multiples of random distribution.

symmetric tilt boundary positions, considering the measurement resolution. The distribution was quite similar at 60°, though the {110} symmetric tilt boundary peaks became highly pronounced with a population of ~31 and ~19 MRD for Steel A and Steel B, respectively (Fig. 8c and 8f).

The distribution of intervariant boundary plane character about the [101] misorientation axis revealed a similar trend as a function of misorientation angle for both martensitic microstructures (Fig. 9). For a misorientation angle of 10.5°, the distribution revealed multiple peaks at {110} positions, though the strongest one was centered at the twist boundary position of {011}||{011} (Fig. 9a and 9d). At 49.5°, the distribution markedly changed, showing only a single peak at the {011}||{011} twist boundary position with a significant increment in the intensity for both martensitic microstructures (Fig. 9b and 9e). Though the characteristics of the distribution did not vary with an increase of misorientation angle to 60°, the intensity of the maxima at the (011) twist boundary position increased from ~27 to ~200 MRD and ~18 ~232 MRD for Steel A and Steel B, respectively (Fig. 9c and 9i).

The intervariant boundary plane character distribution maps for other high index misorientations displayed either one or multiple peaks, centered at or close to the {110} positions for both martensitic steels (Fig. A.1). In general, they did not reveal any twist or tilt character, though they may represent these characters in other representations [22]. The populations of high index intervariant boundaries were largely lower than that of boundaries with [110] and [111] misorientations. However, boundaries with the 50.5°/[-7 -5 5] and 57.2°/[-3 5 6] misorientations had maxima of ~20 and ~36 MRD, respectively, both having a single peak very close to (8 -1 6) ||(-8 6 1) (Fig. A.1. f and i).

3.1.4. Connectivity of the intervariant boundary network

The intervariant boundary network connectivity for both martensitic microstructures was determined using two-dimensional EBSD data through the homology metrics approach [20]. Here, two topological parameters (i.e., B_0 and B_1, known as Betti numbers), are needed to measure the grain boundary network connectivity. B_0 refers to separate boundary segments and B_1 is the number of enclosed paths/loops of boundaries. The ratio of B_0/B_1 defines the inverse connectivity of the boundary network, which can be measured based on misorientation angle and/or lattice misorientation (i.e., misorientation angle/axis, Fig. 10). The increase of misorientation angle threshold eliminated more boundaries from the network, which resulted in a decrease in the connectivity of boundary network (i.e., increase in the B_0/B_1 value, Fig. 10a-i). In general, the inverse connectivity as a function of misorientation angle was qualitatively similar for both steels. However, the grain boundary network of Steel A appeared to be more connected up to a misorientation angle threshold of 45°, beyond which Steel B showed slightly higher boundary network connectivity (Fig. 10i). To measure

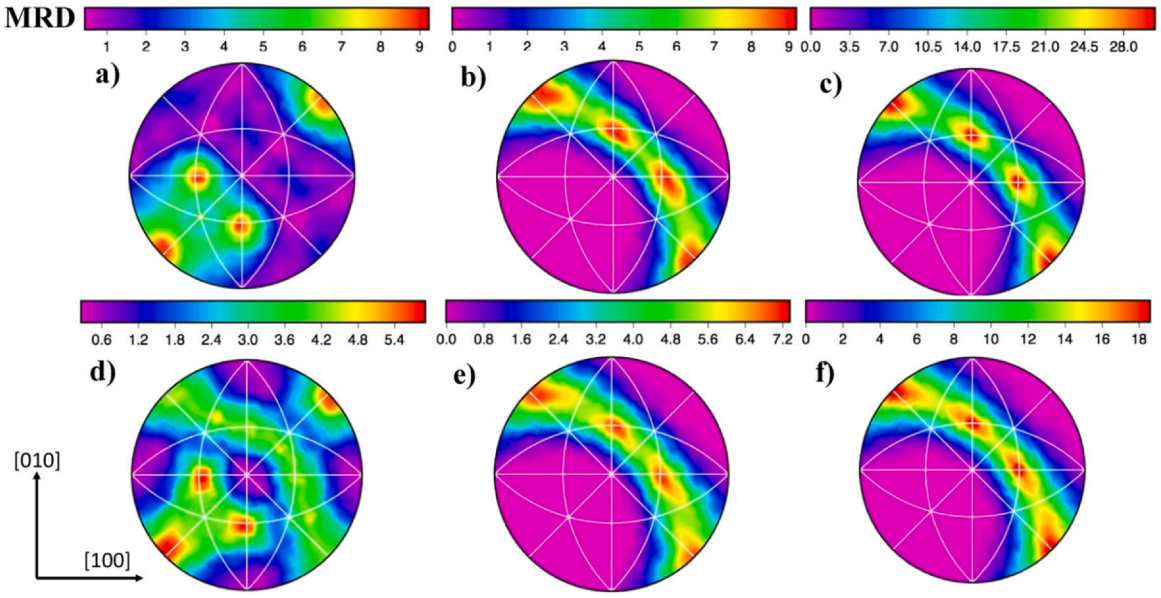

Fig. 8. The distribution of boundary plane normals for boundaries in martensitic microstructures, having misorientation angles about [111] for a–c) Steel A and d–f) Steel B. a, d) 10.5°/[11-1], b, e) 49.5°/[-1-11], and c, f) 60°/[11-1]. MRD represents multiples of random distribution.

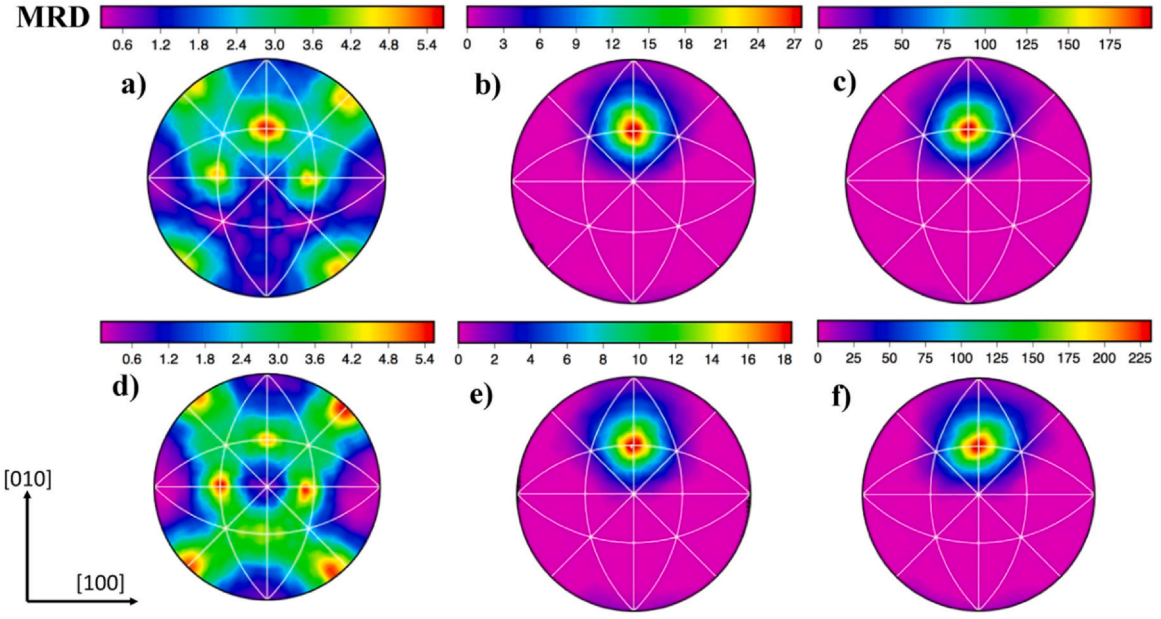

Fig. 9. The distribution of boundary plane normals for boundaries in martensitic microstructures, having misorientation angles about [011] for a–c) Steel A and d–f) Steel B. a, d) 10.5°/[0-1-1], b, e) 49.5°/[011], and c, f) 60°/[011]. MRD represents multiples of random distribution.

the connectivity of the intervariant boundary network, boundaries with misorientations in the range of 22–46° were initially excluded from the data set as these boundaries were largely inherited from the prior austenite grain boundaries based on the K-S OR (Table 3). Afterwards, the B_0/B_1 ratio was plotted as a function of misorientation angle and/or <110> and <111> misorientation axes, which represents the connectivity of different {110} boundary types, namely all {110} boundary types, {110} twist and {110} tilt types, respectively. The trend of the {110} boundaries network was similar to the overall boundary network, where Steel A revealed higher connectivity at a misorientation angle of less than 45° and Steel B became more connected beyond this (Fig. 11i-j). In terms of boundaries with the {110} twist character, it appeared that Steel B had better connectivity than Steel A for all misorientation angles. However, the connectivity of boundaries with the {110} tilt character was slightly greater for Steel A compared with Steel B for the entire misorientation angle range (Fig. 10j).

4. Discussion

In the current study, it appears that the change in Mn concentration significantly alters the intervariant boundary network characteristics (i.e., population, plane orientation and connectivity) of lath martensite formed upon water-quenching. The most striking observations are the length fraction of 60°/[011] and 60°/[111] intervariant boundaries, where the former is much greater for Steel B (i.e., 46%) compared with Steel A (i.e., 32%, Fig. 6). In contrast, the population of intervariant boundaries with 60°/[111] is relatively higher in Steel A (i.e., 5%) than Steel B (i.e., 2.3%, Fig. 6). Generally, the grain boundary population can be affected by several factors such as

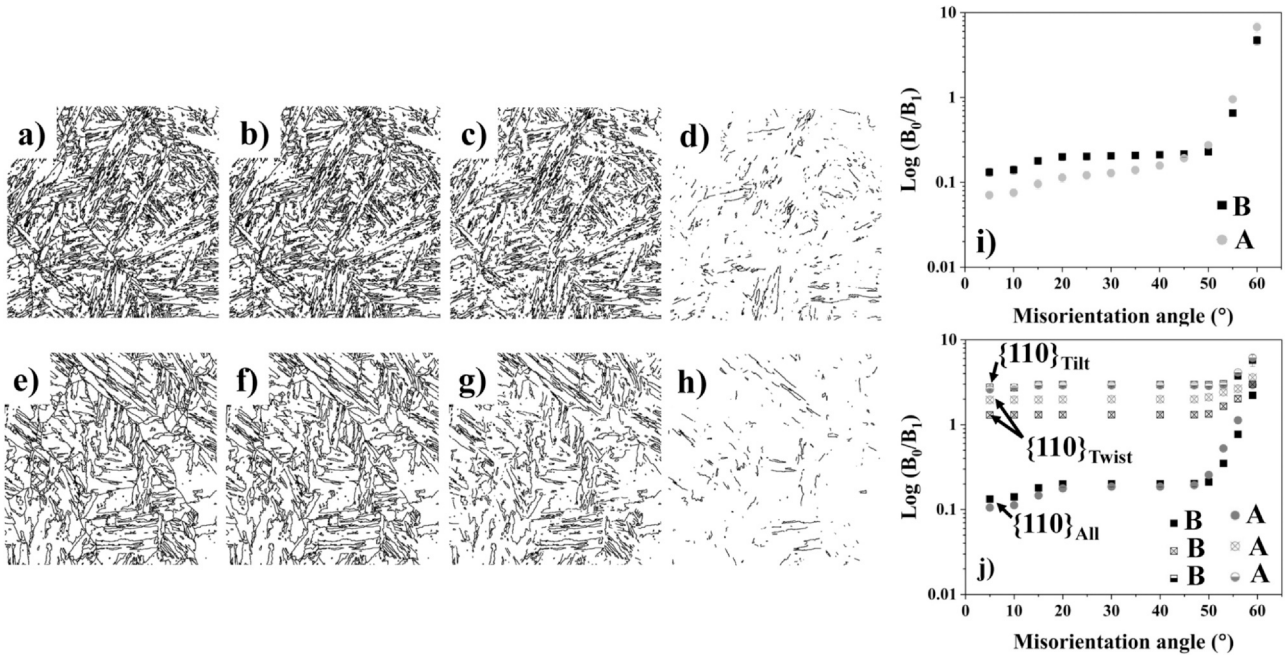

Fig. 10. Threshold boundary maps of Steel B (a–d) and Steel A (e–h) microstructures considering all boundaries with misorientation angle (a, e) >20°, (b, f) >40°, (c, g) >55°, (d, h) >60°. The inverse connectivity of boundary network structure as a function of misorientation angle threshold for all boundaries (i) and (110) plane types (j) for both lath martensitic microstructures. A and B represent Steel A and Steel B, respectively.

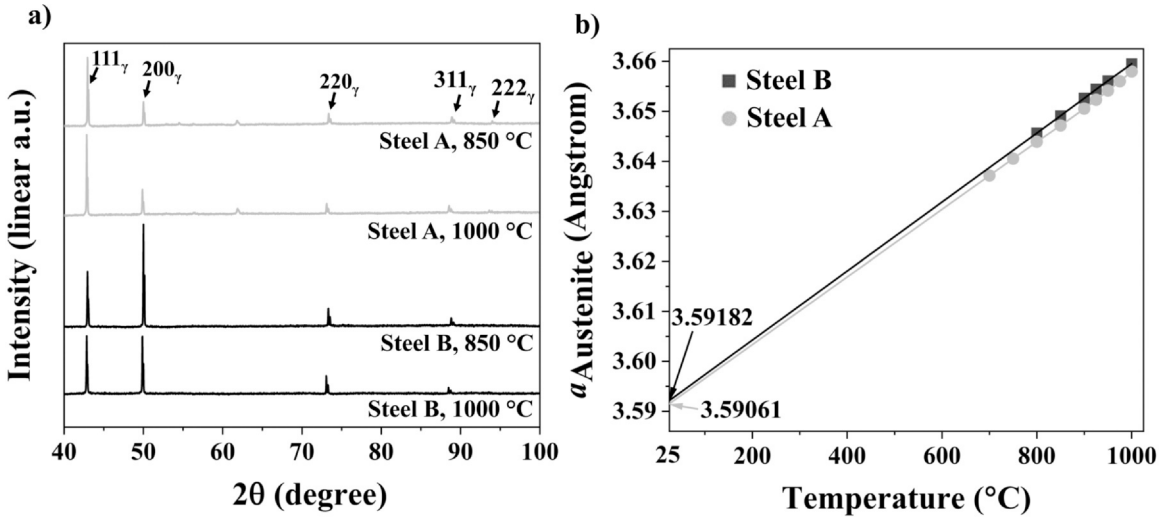

Fig. 11. a) In-situ XRD results of Steel A and Steel B at 1000 °C and 850 °C, showing austenite peaks in which Steel A XRD profiles showed additional peaks associated with NbC and NbN phases, b) determined lattice parameter of austenite phase at different temperatures, which were extrapolated to determine the lattice parameter of austenite at room temperature (i.e., 25 °C); a.u – linear arbitrary unit, $\alpha_{Austenite}$ – lattice parameter of austenite.

grain boundary energy [19,20,23,24], crystallographic texture [25], phase transformation mechanism [20,25], initial grain size [26–29], and chemical composition [20,25,30–35]. The phase transformation mechanism and crystallographic texture are ruled out here, as both steels have undergone a similar martensitic transformation (i.e., shear), which leads to a known transformation texture based on the K-S OR [36]. In the martensitic transformation, the grain boundary characteristics (i.e., population and plane) are largely influenced by the phase transformation constraints rather than their energy [20], as discussed later. The reduction in prior austenite grain size may restrict the number of variants formed within a given austenite grain, altering the block, packet, and ultimately the intervariant boundaries population [26,35,37]. Despite a variation in the prior austenite grain size between Steel B (~32 ± 7 μm) and Steel A (~45 ± 7 μm), the difference in their packet size and block size is insignificant (Table 2). This suggests that the difference in prior austenite grain size do not have a noteworthy influence on the intervariant boundary network, if any, in the current study.

The chemical composition can significantly alter the lattice parameters of both parent austenite and daughter products (i.e., martensite). This variation results in different lattice correspondence between the austenite and martensite phases altering the lattice distortion and inhomogeneous shear during the transformation. Subsequently, the martensitic phase transformation mechanism (i.e., dislocation slip vs twinning) can be influenced, leading to the formation of distinct variant selection arrangement/s to self-accommodate the transformation strain [38,39]. Among different alloying elements, interstitial elements such as carbon have a substantial

Table 4
The typical calculated crystallographic sets for Steel A and Steel B.

	Steel A	Steel B
Lattice parameters	a_α = 2.87892, a_γ = 3.59061	a_α = 2.86817, a_γ = 3.59182
Lattice invariant Shear system, S1 and S2	S1: $<\bar{1}\bar{1}0>_\gamma$ $(\bar{1}11)_\gamma$, S2: $<\bar{1}\bar{1}0>_\gamma$ $(1\bar{1}2)_\gamma$	
Bain strain, B	$\begin{bmatrix} 1.1339 & 0 & 0 \\ 0 & 1.1339 & 0 \\ 0 & 0 & 0.8018 \end{bmatrix}$	$\begin{bmatrix} 1.1293 & 0 & 0 \\ 0 & 1.1293 & 0 \\ 0 & 0 & 0.7985 \end{bmatrix}$
Shear direction	$<-0.9200, 0.0682, -0.2850>_\gamma$	$<0.0663, -0.9103, -0.4086>_\gamma$
Rotation matrix, R	$\begin{bmatrix} 0.9981 & -0.0054 & -0.0609 \\ 0.0147 & 0.9881 & 0.1532 \\ 0.0594 & -0.1538 & 0.9863 \end{bmatrix}$	$\begin{bmatrix} 0.9841 & -0.0742 & -0.1608 \\ 0.0604 & 0.9942 & -0.0889 \\ 0.1664 & 0.0777 & 0.9826 \end{bmatrix}$
Shear Magnitude	0.2951 S_1 = 0.2850, S_2 = 0.1259	0.2895 S_1 = 0.2850, S_2 = 0.1164
Shape deformation, F	$\begin{bmatrix} 1.1159 & 0.1343 & 0.0539 \\ 0.0180 & 0.9996 & -0.0539 \\ -0.2111 & 0.0936 & 0.9095 \end{bmatrix}$	$\begin{bmatrix} 1.0009 & 0.0224 & -0.0536 \\ 0.1293 & 1.1069 & 0.0536 \\ 0.0977 & -0.2058 & 0.9058 \end{bmatrix}$
Habit plane	$<0.4561, 0.5156, 0.7253>_\gamma$	$<0.4346, 0.5321, 0.7267>_\gamma$

influence on the lattice parameter [35]. However, the carbon level of these steels is very low and their difference is negligible (Table 1). The main alloying element difference in the current steels is the addition of Mn in Steel A to partially replace Ni. The addition of Mn is shown to promote the internal-twinning during martensite transformation in Fe-0.25C and Fe-0.25C-Ni systems [40], which is ultimately expected to enhance the 60°/[111] intervariant boundary population. However, there is no evidence of transformation twins in the current martensitic microstructures (Fig. 3a), suggesting that the martensitic transformation for both steels takes place through dislocation slip rather than twinning. To understand the role of chemical composition (i.e., Mn) on the grain boundary network, it is, therefore, essential to explore the variant selection arrangement/s that alleviate the accommodation of the phase transformation strain in both steels using the K-S OR according to the phenomological theory of the martensitic transformation.

4.1. Rationalization of the martensitic microstructure

Martensite variant selection is mostly associated with shape strain minimization, which is directly related to the lattice parameter of the parent austenite and martensite [33,41]. An increase in the amount of alloying elements can influence the lattice parameter of parent austenite [38]. The change in crystal lattice structure during martensite transformation produces large macroscopic shape strains. The developed transformation strain can be accommodated by an invariant lattice strain, which leaves a plane (i.e., the habit plane) undistorted and un-rotated. The lattice invariant shear is processed by either slip or twinning and they are usually observed within the lath martensite substructure [39]. Which of the slip or twinning mechanisms is introduced during the transformation is strongly associated with the lattice parameters of the parent and daughter phases and, thus, influenced by the alloy composition [42,43]. The phenomenological theories based on the occurrence of simple shear are successful on predicting the crystallographic parameters of martensite transformation in many alloys [44–49]. However, considering the occurrence of two simultaneous and unrelated lattice invariant shears are shown to be more successful in describing the crystallography associated with the shear transformation [41,49].

The presence of two lattice invariant shears is an effective mechanism to reduce the shape strain associated with the transformation. However, the shear component of the shape change is still present and requires accommodation to maintain the material integrity. This requirement results in the formation of different martensite plates within a systematic order giving a characteristic morphology of martensite in the microstructure. Such martensite variant grouping is known as the self-accommodation phenomenon, that can induce a characteristic microstructure, texture and intervariant boundaries during the martensite transformation [50].

In the current study, the phenomenological theory of martensite considering double invariant lattice shears [41,51,52] is utilized to calculate the shape deformation, shear magnitude and the habit plane for both steels. Due to the absence of retained austenite in the as-quenched microstructures, both steels were subjected to in-situ XRD experiments to form a single-phase austenite and measure their lattice parameters at high temperature. This involved reheating the steel to 1000 °C and holding for 30 min followed by cooling. The XRD pattern was recorded during the cooling stage after holding for 30 min at different isothermal temperatures between 1000 °C and 700 °C. The resultant XRD patterns of Steel B showed crystallographic peaks of austenite phase, as shown in Fig. 11a, which were used to calculate the lattice parameter of austenite at different temperatures. A similar approach was applied for Steel A (Fig. 11a). The calculated lattice parameters of both steels were plotted against the temperature, which were extrapolated linearly to room temperature (i.e., 25 °C) to determine the lattice parameter of austenite (Fig. 11b). The resultant lattice parameter of austenite at room temperature was 3.59061 ± 0.00057 Å and 3.59182 ± 0.00028 Å for Steels A and B, respectively. This approach is valid because the lattice parameter varies linearly with temperature [53]. The lattice parameter of martensite was also measured 2.87892 ± 0.00008 Å and 2.86817 ± 0.00005 Å for Steels A and B, respectively, determined by using XRD at room temperature (Fig. 3). The high temperature XRD patterns of Steel A showed some low intensity peaks (in the 2θ range of 55–65°) associated with the evolution of minor fractions of possible Cr_2N and NbN precipitates [54,55] (Fig. 11a). However, given a very good linear relationship of lattice parameters variations shown in Fig. 11b, the influence of this precipitation on the lattice parameter of austenite during martensite is neglected.

According to the double lattice invariant shear theory [41,43,51], the shape deformation, F, occurring during the martensite transformation can be described as the product of a complementary rigid body rotation, R, a pure deformation or Bain strain, B, and two lattice invariant shears denoted by S1 and S2.

$$F = RBS_2S_1 \tag{5.1}$$

The current calculation was carried out assuming the two shear systems, which has been previously shown to predict the correct habit plane of $(557)_\gamma$ for low carbon steels [30,52]. The considered shears were the twinning shear $<\bar{1}\bar{1}0>_\gamma$ $(\bar{1}11)_\gamma$ (within the austenite lattice) and the supplementary shear $<\bar{1}\bar{1}0>_\gamma$ $(1\bar{1}2)_\gamma$. First, the shape deformation matrix, shear direction and magnitude was calculated (Table 4). Finally, the predicted habit plane in the operating double shear system was also compared with the experimentally observed $\{557\}_\gamma$ habit plane [56]. According to the current

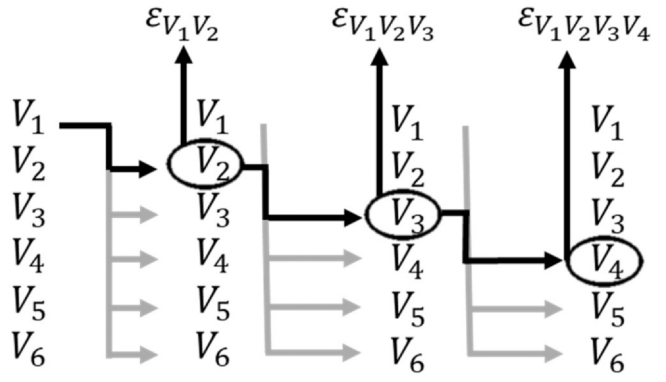

Fig. 12. The calculation of ε_{VM} for different 2, 3, and 4 variant cluster combination using Von Mises criteria [55].

calculation, the predicted habit planes were 4.450° and 3.032° away from the experimental Steels A and B habit planes, respectively.

Furthermore, the shape deformation tensors (F_{ij}) of the possible family of variants sharing the same habit plane were identified and the corresponding strain tensors (T_{ij}) were calculated in the following way:

$$(T_{ij}) = \frac{F_{ij}{}^{t}F_{ij} - I}{2} \tag{5.2}$$

Where, I represents the unit matrix and $F_{ij}{}^{t}$ is the transpose of shape deformation tensor. Finally, the degree of the self-accommodation for different variant combinations can be determined from the Von-Mises equivalent strain (ε_{VM}). The Von-Mises equivalent strain is computed from the overall transformation strain tensors for different variant combinations (i.e., 2-, 3- and 4-variant cluster combinations) in the following way:

$$\varepsilon_{VM} = \sqrt{\frac{3}{2}((T_{11}^2 + T_{22}^2 + T_{33}^3) + \frac{1}{2}(4T_{12}^2 + 4T_{13}^2 + 4T_{23}^2))} \tag{5.3}$$

Fig. 12 shows the different possible combinations of stress tensors considered in this study [57]. There are 30, 120, and 360 different possible 2-, 3-, and 4-variant combinations within a family of variants that share same habit plane (i.e., martensite packet), respectively. The combination of the ε_{VM} as a result of variant clustering leads to calculation of average ε_{VM} (i.e., ε_{ave}). The combinations with the minimum ε_{ave} for both martensitic steels were given in Table 5. For Steel B, the three-variant cluster had the minimum ε_{ave}(ε_{ave} = 0.0300), promoting the grouping of $V_1V_3V_5$ within a martensite packet. On the other hand, the martensite variants of Steel A had the smallest ε_{ave} for the four variant clusters (ε_{ave} = 0.0347) of $V_1V_2V_3V_5$ combination.

The change in chemical composition (i.e., Mn addition) between these martensitic steels influences the respective austenite and martensite lattice parameters, ultimately affecting the inhomogeneous shear magnitude (Table 4). The phenomenological theory of martensite calculation indicates that the chemical composition change in the steel alters the variant arrangement from 3-variant clustering in Steel B to 4-varaint clustering in Steel A to minimize ε_{ave} (Table 5). The 3-variant clustering largely leads to the formation of 60°/[110] intervariant boundaries, though the 4-varaint clustering also encourages the formation of 60°/[111] boundaries that forms as a result of impingement of two consecutive variants (e.g., V_1V_2, V_2V_3). This is consistent with the measured intervariant boundary population distribution of both martensitic steels (Fig. 6), where the population of 60°/[111] boundaries increases at the expense of 60°/[110] in Steel A in comparison with the Steel B. It should be mentioned that the three- and four-variant clusters minimum shear strains are very close, which can be promoted by local

Table 5
The Von-Mises equivalent strain calculated for different combinations of variant cluster arrangements in the martensitic transformation for Steels A and B.

Steel	Two variants				Possible intervariant boundaries in a packet	Three variants			Possible intervariant boundaries in a packet	Four variants			Possible intervariant boundaries in a packet
Steel A	$Minimum\varepsilon_{ave}$	0.0485	V_2V_5	V_3V_4	10.5°/[110] 60°/[111]	$Minimum\varepsilon_{ave}$	0.0357	$V_1V_3V_5$	60°/[110]	$Minimum\varepsilon_{ave}$	0.0347	$V_1V_2V_3V_5$	60°/[110] 60°/[111]
Steel B	$Minimum\varepsilon_{ave}$	0.0540	V_1V_2	V_3V_6	60°/[110] 60°/[111]	$Minimum\varepsilon_{ave}$	0.0300	$V_1V_3V_5$	60°/[110]	$Minimum\varepsilon_{ave}$	0.0373	$V_1V_2V_3V_5$	60°/[110] 60°/[111]

inhomogeneous lattice strains. Therefore, both variant arrangements can be expected in the microstructure of martensitic steels but with a lower frequency for the non-dominant cluster.

4.2. Intervariant boundary character distribution

The five-parameter analysis of both martensitic microstructures reveals that most intervariant boundaries are terminated on {110} planes (Figs. 8–9). It is well known that the relative areas of grain boundary planes for polycrystalline materials that evolve through normal grain growth have an inverse relationship with their energies [19,20,23,24,58]. However, the characteristics of the grain boundary plane character distribution in martensitic microstructures formed through shear transformation appears to differ from the polygonal ferritic microstructure produced through the grain growth and/or diffusional phase transformation processes [20,23,25]. The grain boundary plane character distribution for 60°/[111], for example, exhibits maxima at the position of the {110} symmetric tilt boundary for both martensitic microstructures (Fig. 8c, f), which is not consistent with the distribution reported for polygonal ferrite, that has maxima on the {112} symmetric tilt boundaries that have the least energy [23,25]. According to the K-S OR, the close packed plane of parent austenite (i.e., $\{111\}_{\gamma}$) is parallel to the closed packed plane of martensite (i.e., $\{011\}_{\gamma}$) upon phase transformation. Hence, the impingement of two martensite variants within a given parent austenite results in an intervariant boundary terminated at the $(011)_{\alpha'}$ plane. The current observation is consistent with the previous works [20,59], where the crystallographic constraints associated with the martensitic/shear transformation mostly promotes the {110} planes during the transformation, which is not necessarily the lowest energy configuration.

4.3. Connectivity of grain boundary network

The determination of the inverse connectivity of the boundary network (B_0/B_1) as a function of misorientation angle ultimately reveals the characteristics of the intervariant boundary network of the lath martensitic microstructures. Though the microstructure is lath martensite, there is a considerable difference in the inverse connectivity of the boundary network between both martensitic steels (Fig. 10i). This difference diminishes with an increase in the threshold misorientation angle. At higher misorientation angles (>50°), the boundary network connectivity for both steels decreases significantly, but the boundary network of Steel A becomes relatively less connected than that of Steel B. However, the determination of the connectivity of a specific crystallographic plane is more important, as it directly governs the properties [12]. According to the intervariant boundary plane character distribution, most of the intervariant boundaries/interfaces terminate on {110} or near {110} planes (Figs. 8–9). Therefore, the exclusion of boundaries with misorientation angles in the range of 22–46° (i.e., prior austenite grain boundaries) leads to the measurement of the connectivity of boundaries with the {110} orientation as a function of misorientation angle. The resultant inverse connectivity of {110} planes shows a negligible difference at low misorientation angles between the martensitic steels (Fig. 10j). Since the boundary plane character distribution of boundaries with [111] and [110] axes is mainly characterized as {110} symmetric tilt and {110} twist plane types, respectively, the determination of connectivity of these boundaries ultimately results in the determination of the connectivity of specific {110} plane type/s (i.e., twist and/or tilt boundaries). The inverse connectivity as a function of misorientation angle shows a similar trend for boundaries with {110} symmetric tilt and {110} symmetric twist planes for both steels (Fig. 10j). The former shows the least connectivity for both steels and there is no considerable difference in the connectivity between Steels A and B. Interestingly, the {110} symmetric tilt boundaries are less connected for Steel A when compared to Steel B, which is in good agreement with the low fraction of [110] boundaries for Steel A (Fig. 6). As observed in the previous study [12], except {110} tilt boundaries, the connectivity of other {110} type boundary networks converge beyond the 50° misorientation angle (Fig. 10j). These changes are clearly reflected in the intervariant boundaries/interfaces fraction (Fig. 6). Therefore, the current study strongly suggests that the grain boundary network (i.e., population and connectivity) of lath martensite microstructure can be manipulated by changing the chemical composition of the steel (i.e., addition of Mn).

5. Conclusions

In the current study, the role of chemical composition on the grain boundary network developed upon martensitic phase transformation in a commercial (17-4PH) and Mn bearing precipitation hardenable stainless steels was investigated. The followings are the notable findings:

1) The misorientation angle distribution of both martensitic steels revealed a qualitatively similar distribution, which was closely associated with the K-S OR. The addition of Mn, though, reduced the number of boundaries with a 60° misorientation angle, which corresponded well with a decrease in the population of the 60°/[011] intervariant boundary.
2) The change in the grain boundary population was explained using the phenomenological theory of martensite, which showed that while 3-variant clustering (i.e., $V_1V_3V_5$) was preferred in the 17-4PH steel, the change in lattice parameter caused by the addition of Mn led to a preference for the 4-varaint clustering (i.e., $V_1V_2V_3V_5$); the 4-varaint arrangement minimized the strain associated with the displacive martensitic transformation in the Mn bearing steel. The 4-variant clustering also promoted the population of 60°/[111] boundaries at the expense of 60°/[011] boundaries.
3) The changes in local variant selection mechanism affected the connectivity of grain boundary network. For example, the connectivity of {110} twist boundaries was reduced with an addition of Mn, most likely due to a decrease in its decreased population. This suggests that the grain boundary network characteristics (i.e., population and connectivity) of lath martensitic microstructure can be manipulated by changing the chemical composition of the steel.
4) The intervariant boundary plane distribution was anisotropic for both martensitic steels, terminating on {110} planes, instead of lower energy {112} planes. The preference for {110} planes results from the mechanism of the displacive phase transformation.
5) For both martensitic steels, the distribution of intervariant boundary planes with the misorientation axis of [110] and [111] were largely centered on {110} twist and {110} symmetric tilt positions, respectively,

CRediT authorship contribution statement

Vinothkumar Govindaraj: Methodology, Investigation, Writing – original draft. **Ehsan Farabi:** Formal analysis, Validation, Writing – review & editing. **Sitarama Kada:** Methodology, Writing – review & editing. **Peter Hodgson:** Supervision, Writing – review & editing. **Rajkumar Singh:** Supervision, Writing – review & editing. **Gregory Rohrer:** Programming, Writing – review & editing. **Hossein Beladi:** Supervision, Conceptualization, Methodology, Writing – review & editing.

Declaration of Competing Interest

The authors declare that they have no known competing financial interests or personal relationships that could have appeared to influence the work reported in this paper.

Acknowledgements

The authors wish to acknowledge SAAR LOHA, India and Bharat Forge, India for their support in development of materials and subsequent processing. Deakin University's Advanced Characterization Facility is acknowledged for use of the EBSD instruments. The authors also thank to MME, IIT MADRAS for the TEM characterization. The authors also thank to Bharat Forge, India for the funding and support provided to carry out this research.

Appendix A Phenomenological theory of martensitic transformation

Greninger-Troiano [60] showed that the martensite transformation undergoes a uniform shear on a certain austenite plane. Such macroscopic shear would have resulted into a triclinic lattice formation from the fcc austenite phase. Therefore, the presence of another shear needs to be considered to produce the bct lattice within the martensite transformation. In the double shear mechanism, the shape change is progressed through a macroscopic shear and an undetectable second microscopic shear [41,51,61]. The microscopic shear is accompanied within a shear plane and direction and is observed as striations on the surface of martensite plate. The double shear mechanism is further supported by the Bowles and Mackenzie (B-M theory) [44–46] and by Wechsler, Lieberman, and Read (W-L-R theory) [47–49]. Although they are independent approaches, all are equivalent and considers three main point; presence of an undistorted and un-rotated plane (invariant plane), Bain distortion and a lattice invariant shear (complementary shear) for producing an undistorted plane.

The crystallographic changes of the parent and daughter lattices produces a homogeneous deformation (Bain distortion). Considering the parent lattice as the Bain cone in Fig. A.2, the initial position of the undistorted planes, P and Q resulting from a single lattice invariant shear is shown in Fig. A.2a. The total shape deformation makes the planes cut the cone into four undistorted lines. For the transformation to occur by two lattice invariant shear (double shear mechanism), instead of a pair of undistorted planes a double shear cone is produced. In this case, double shear cone can have three distinct configurations producing four, two and no undistorted lines (Fig. A.2b–d). Finally, a pair of shear magnitudes that leaves an invariant angle between the undistorted lines needs to be selected. This choice of shear magnitudes in algebraic form is discussed in the following.

In general theories, the shape deformation, lattice rotation and deformation can be represented in a 3×3 matrix form of ***P, R and B, respectively, so that the total shape deformation can be represented as*** $F = RBP$. Considering the double shear mechanism [41,51,61], the P can be replaced by two shears denoted as S_1 and S_2.

$$F = RBS_2S_1 \tag{A.1}$$

The 3× 3 shear matrices are given by $S = \delta_{ij} + gl_im_j$, where δ_{ij} is the Kronecker delta, g is the shear magnitude on the m_j plane along the l_i shear direction. Also, the deformation matrix representing the Bain strain, which carries the fcc-austenite lattice to bcc α-lattice in an orthonormal basis can be given by:

$$B = \begin{Bmatrix} \eta_1 = c_h/\sqrt{2}\,a_b & 0 & 0 \\ 0 & \eta_2 = \sqrt{3}\,a_h/\sqrt{2}\,a_b & 0 \\ 0 & 0 & \eta_3 = a_h/a_b \end{Bmatrix} \tag{A.2}$$

The undistorted plane should maintain it principle as equal to unity. This can be expressed by the determinant equation

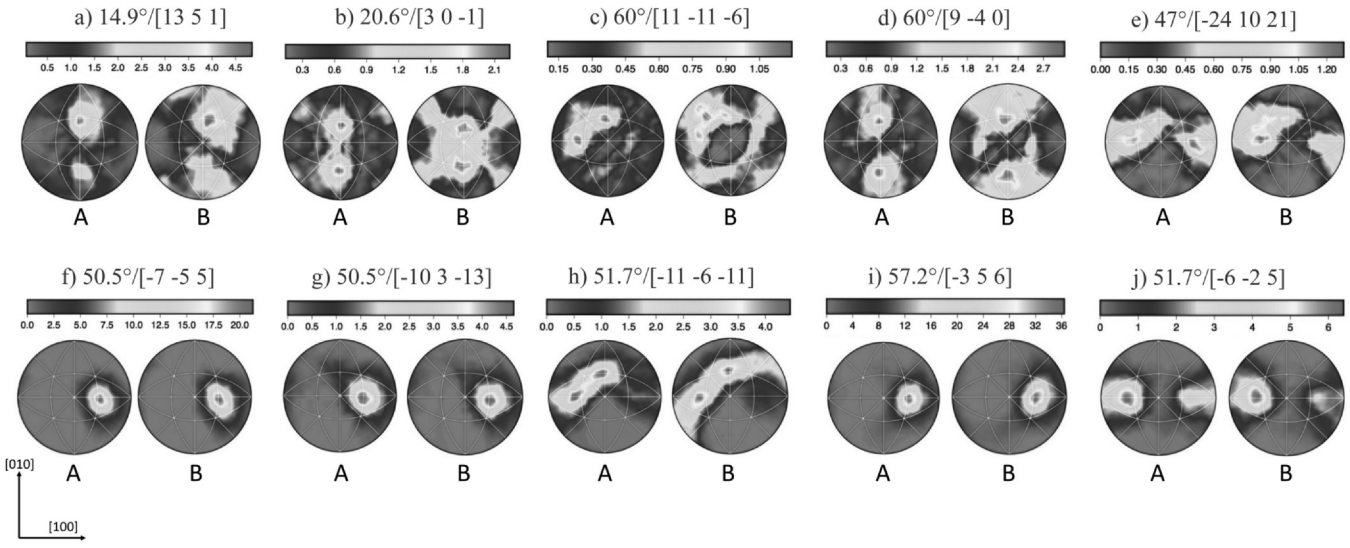

Fig. A.1. The distribution of boundary plane normals with different lattice misorientations associated with the K-S OR for both martensitic steels. A and B represent Steel A and Steel B, respectively.

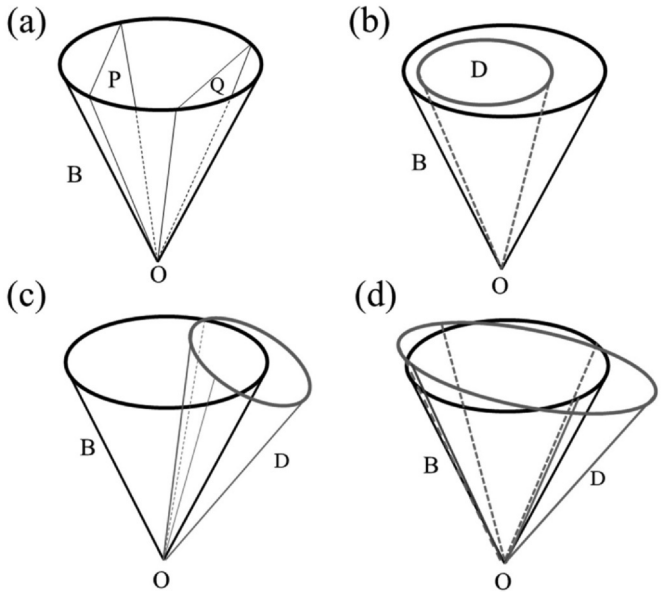

Fig. A.2. Illustration of the undistorted lines within the bane cone (indicated as B in the figures). (a) The present four undistorted line developed by the invariant plane P and Q developed by a single lattice invariant shear. (b-d) the possible formation of undistorted lines developed through a double shear cone (indicated by D). in (b) there is no intersection but in (c) and (d) two and four undistorted line is present, respectively [58].

$$|F^T F - I| = 0 \tag{A.3}$$

where the F^T is the transpose of the shape deformation *F and I is the unit, matrix. Substituting the equation 1 into the detriment, the following quadratic equation for the magnitude* g_1 of the first shear would be developed.

$$Ag_1^2 + 2Bg_1 + C = 0 \tag{A.4}$$

Where

$$A = Q_{11} + Q_{31}^2 - Q_{33}Q_{11} \tag{A.5}$$

$$B = Q_{12} + Q_{23}Q_{31} - Q_{12}Q_{33}$$

$$C = Q_{11} + Q_{22} + Q_{33} + Q_{12}^2 + Q_{23}^2 + Q_{31}^2 - Q_{11}Q_{22} - Q_{22}Q_{33} - Q_{33}Q_{11} + \eta_1^2\eta_2^2\eta_3^2 - 1$$

Here, R has been eliminated in the transposition as the elements of the Q can be given as $Q = S_2^{*T}P^{*T}P^{*}S_2^{*}$. $P^{*}$and S_2^{*} are the similarity transformation of the P and S_2 to the orthonormal basis defined by the vectors $I^1 \times m^1$ (for the first shear plane and direction). Knowing the lattice parameters, correspondence and the shear planes and directions, the shear magnitudes g_1 and g_2 would be the only unknown in the equation. When solved, two values of g_1 would be provided for a given g_2 and vice versa. When the appropriate pair of lattice invariant shear is selected, the habit plane can be defined by considering two unit vectors; u of the parent and the corresponding vector $v = S_2S_1u$ obtained by the double shear deformation, S_2S_1. Equating the length of these two vectors we obtain the equation of the double-shear cone,

$$v^T = (I - W)v = 0 \tag{A.6}$$

The elements of the W are given by,

$$W_{ij} = \delta_{ij} - g_2(l_i^2m_j^2 + l_j^2m_i^2) - g_1(l_1^1m_j^1 + l_j^1m_i^1) + \quad g_1g_2([m_j^1l_j^2]\{l_i^1m_j^2 + l_j^1m_i^2\} + [l_j^1l_j^2] \times \{m_i^1m_j^2 + m_j^1m_i^2\})$$
$$- g_1g_2[m_j^1l_j^2] \times (2g_2[l_j^1l_j^2]m_i^2m_j^2 + g_1\{m_i^2m_j^2 + m_j^1m_i^2\}) + g_1^2g_2^2[m_j^1l_j^2]m_i^2m_j^2 \tag{A.7}$$

The Bain cone equation can also be obtained by equating the lengths of the vectors v and Bv to give

$$v^T(I - B)v = 0 \tag{A.8}$$

This means that v is a unit vector and can be described as below:

$$v^Tv = 1 \tag{A.9}$$

The vector v satisfying the equations (6), (8) and (9) can be regarded as the undistorted line of the shape deformation. Four distinct solution for v is developed for each pair of shear magnitudes g_1 and g_2. The solution for the parent u vector is now given by $u = S_1^{-1}S_2^{-1}v$. Two undistorted lines u_1 and u_2, derived from v_1 and v_2 is then defines the habit plane *h. To this end they must be accommodating the* $u_1^Tu_2 = v_1^TB^2v_2$ relation. Of course, in general for a given value of g_2, we obtain two values of g_1 from equation (3), and each of these provides two possible habit planes.

The total shape deformation F of the martensite transformation can be calculated as following

$$F_{ij} = \delta_{ij} + \mu d_i h_j \tag{A.10}$$

where μd is the displacement at unit distance from the habit plane *h. Thus, the determinant of F, which defines the ratio of the volumes of the product and parent structures, is given by* $1 + \mu d_i v_j$. The determinants of F and B are equal and therefore,

$$\mu d_i v_j = \eta_1 \eta_2 \eta_3 - 1 \tag{A.11}$$

The matrix $Z = F^T F$ can be defined. The trace of Z which is $T = \mu^2 + 2\mu d_i h_i + 3$ and based on equation 9 we have

$$\mu^2 = T - 2\eta_1 \eta_2 \eta_3 - 1 \tag{A.12}$$

Therefore, the following can be obtained,

$$d_\alpha = (Z_{\alpha\alpha} - \mu^2 v_\alpha^2 - 1)(2\mu v_\alpha)^{-1} \tag{A.13}$$

When substituting for μ and d_α into equation 10 we can have F and the D = RB, giving the lattice deformation.

References

[1] C. Servant, E.H. Gherbi, G. Cizeron, TEM investigation of the tempering behaviour of the maraging PH 17.4 Mo stainless steel, J. Mater. Sci. 22 (7) (1987) 2297–2304.
[2] H. Nakagawa, T. Miyazaki, H. Yokota, Effects of aging temperature on the microstructure and mechanical properties of 1.8 Cu-7.3 Ni-15.9 Cr-1.2 Mo-low C, N martensitic precipitation hardening stainless steel, J. Mater. Sci. 35 (9) (2000) 2245–2253.
[3] U. Viswanathan, S. Banerjee, R. Krishnan, Effects of aging on the microstructure of 17-4 PH stainless steel, Mater. Sci. Eng. A 104 (1988) 181–189.
[4] M. Murayama, K. Hono, Y. Katayama, Microstructural evolution in a 17-4 PH stainless steel after aging at 400C, Metall. Mater. Trans. A 30 (2) (1999) 345–353.
[5] C. Hsiao, C. Chiou, J. Yang, Aging reactions in a 17-4 PH stainless steel, Mater. Chem. Phys. 74 (2) (2002) 134–142.
[6] J. Wang, H. Zou, C. Li, S.-y Qiu, B.-l Shen, The effect of microstructural evolution on hardening behavior of type 17-4PH stainless steel in long-term aging at 350C, Mater. Charact. 57 (4–5) (2006) 274–280.
[7] G. Yeli, M.A. Auger, K. Wilford, G.D. Smith, P.A. Bagot, M.P. Moody, Sequential nucleation of phases in a 17-4PH steel: microstructural characterisation and mechanical properties, Acta Mater. 125 (2017) 38–49.
[8] Z. Wang, H. Li, Q. Shen, W. Liu, Z. Wang, Nano-precipitates evolution and their effects on mechanical properties of 17-4 precipitation-hardening stainless steel, Acta Mater. 156 (2018) 158–171.
[9] V. Govindaraj, P. Hodgson, R. Singh, H. Beladi, Precipitation reactions in 12Cr-3Ni-3Mn-3Cu-0.15Nb steel, Mater. Sci. Eng. A 808 (2021) 140909.
[10] S. Watanabe, Y. Takamatsu, N. Sakaguchi, H. Takahashi, Sink effect of grain boundary on radiation-induced segregation in austenitic stainless steel, Journal of Nuclear Materials 283-287 (2000) 152–156.
[11] M. Dollar, H. Gleiter, Point defect annihilation at grain boundaries in gold, Scipta Metallurgica 19 (1985) 481–484.
[12] P. Lejček, S. Hofmann, V. Paidar, Solute segregation and classification of [100] tilt grain boundaries in α-iron: consequences for grain boundary engineering, Acta Materialia 51 (2003) 3951–3963.
[13] F. Humphreys, Hatherly, Recrystallization and Related Annealing Phenomena, Elsevier, Amsterdam, 2004.
[14] E.J.S.B. Hall, Proc. Phys. Soc. 64 (1951) 747.
[15] N.J. Petch, The cleavage strength of polycrystals, Journal of the Iron and Steel Institute 174 (1953) 25–28.
[16] L.C. Lim, T. Watanabe, Grain boundary character distribution controlled toughness of polycrystals—a two-dimensional model, Scipta Metallurgica 23 (1989) 489–494.
[17] T. Watanabe, H. Fujii, H. Oikawa, K.I. Arai, Grain boundaries in rapidly solidified and annealed Fe-6.5 mass% Si polycrystalline ribbons with high ductility, Acta Metallurgica 37 (1989) 941–952.
[18] R.L. Coble, A model for boundary diffusion controlled creep in polycrystalline materials, Journal of Applied Physics 34 (1963) 1679–1682.
[19] G.S. Rohrer, D.M. Saylor, B.E. Dasher, B.L. Adams, A.D. Rollett, P. Wynblatt, The distribution of internal interfaces in polycrystals, Z. Metallkd. 95 (4) (2004) 197–214.
[20] H. Beladi, G.S. Rohrer, A.D. Rollett, V. Tari, P.D. Hodgson, The distribution of intervariant crystallographic planes in a lath martensite using five macroscopic parameters, Acta Mater. 63 (2014) 86–98.
[21] H.M. Flower, T.C. Lindley, Electron backscattering diffraction study of acicular ferrite, bainite, and martensite steel microstructures, Mater. Sci. Technol. 16 (1) (2000) 26–40.
[22] K. Glowinski, A. Morawiec, Twist, tilt, and symmetric grain boundaries in hexagonal materials, J. Mater. Sci. 49 (11) (2014) 3936–3942.
[23] H. Beladi, G.S. Rohrer, The relative grain boundary area and energy distributions in a ferritic steel determined from three-dimensional electron backscatter diffraction maps, Acta Mater. 61 (4) (2013) 1404–1412.
[24] G.S. Rohrer, Grain boundary energy anisotropy: a review, J. Mater. Sci. 46 (18) (2011) 5881–5895.
[25] H. Beladi, G.S. Rohrer, The distribution of grain boundary planes in interstitial free steel, Metall. Mater. Trans. A 44 (1) (2013) 115–124.
[26] S. Morito, H. Saito, T. Ogawa, T. Furuhara, T. Maki, Effect of austenite grain size on the morphology and crystallography of lath martensite in low carbon steels, ISIJ Int. 45 (1) (2005) 91–94.
[27] Y. Prawoto, N. Jasmawati, K. Sumeru, Effect of prior austenite grain size on the morphology and mechanical properties of martensite in medium carbon steel, J. Mater. Sci. Technol. 28 (5) (2012) 461–466.
[28] H.K. Yeddu, Phase-field modeling of austenite grain size effect on martensitic transformation in stainless steels, Comput. Mater. Sci. 154 (2018) 75–83.
[29] C. Celada-Casero, J. Sietsma, M.J. Santofimia, The role of the austenite grain size in the martensitic transformation in low carbon steels, Mater. Des. 167 (2019) 107625.
[30] S. Morito, H. Tanaka, R. Konishi, T. Furuhara, Maki, The morphology and crystallography of lath martensite in Fe-C alloys, Acta Mater. 51 (6) (2003) 1789–1799.
[31] H. Kitahara, R. Ueji, M. Ueda, N. Tsuji, Y. Minamino, Crystallographic analysis of plate martensite in Fe–28.5 at% Ni by FE-SEM/EBSD, Mater. Charact. 54 (4–5) (2005) 378–386.
[32] H. Kitahara, R. Ueji, N. Tsuji, Y. Minamino, Crystallographic features of lath martensite in low-carbon steel, Acta Mater. 54 (5) (2006) 1279–1288.
[33] S. Morito, X. Huang, T. Furuhara, T. Maki, N. Hansen, The morphology and crystallography of lath martensite in alloy steels, Acta Mater. 54 (19) (2006) 5323–5331.
[34] B. Hutchinson, J. Hagström, O. Karlsson, D. Lindell, M. Tornberg, F. Lindberg, M. Thuvander, Microstructures and hardness of as-quenched martensites (0.1–0.5% C), Acta Mater. 59 (14) (2011) 5845–5858.
[35] A. Stormvinter, G. Miyamoto, T. Furuhara, P. Hedström, A. Borgenstam, Effect of carbon content on variant pairing of martensite in Fe–C alloys, Acta Mater. 60 (20) (2012) 7265–7274.
[36] R.K. Ray, J.J. Jonas, Transformation textures in steels, Int. Mater. Rev. 35 (1) (1990) 1–36.
[37] T. Furuhara, K. Kikumoto, H. Saito, T. Sekine, T. Ogawa, S. Morito, T. Maki, Phase transformation from fine-grained austenite, ISIJ Int. 48 (8) (2008) 1038–1045.
[38] Y. Song, X. Li, L. Rong, Y. Li, The influence of tempering temperature on the reversed austenite formation and tensile properties in Fe–13% Cr–4% Ni–Mo low carbon martensite stainless steels, Mater. Sci. Eng. A 528 (12) (2011) 4075–4079.
[39] E.R. Petty, Martensite: fundamentals and technology, edited by ER Petty, (1970).
[40] D.-H. Huang, G. Thomas, Structure and mechanical properties of tempered martensite and lower bainite in Fe− Ni− Mn− C steels, Metall. Trans. 2 (6) (1971) 1587–1598.
[41] P.M. Kelly, Crystallography of lath martensite in steels, Mater. Trans., JIM 33 (3) (1992) 235–242.
[42] S. Miyazaki, K. Otsuka, C. Wayman, The shape memory mechanism associated with the martensitic transformation in Ti·Ni alloys—I. Self-accommodation, Acta Metall. 37 (7) (1989) 1873–1884.
[43] K. Otsuka, C. Wayman, Mechanism of shape memory effect and superelasticity, Shape Mem. Mater. (1998) 27–48.
[44] J. Bowles, J. Mackenzie, The crystallography of martensite transformations I, Acta Metall. 2 (1) (1954) 129–137.
[45] J. Bowles, J.K. Mackenzie, The crystallography of martensite transformations III. Face-centred cubic to body-centred tetragonal transformations, Acta Metall. 2 (2) (1954) 224–234.
[46] J. Mackenzie, J. Bowles, The crystallography of martensite transformations II, Acta Metall. 2 (1) (1954) 138–147.
[47] D. Lieberman, Martensitic transformations and determination of the inhomogeneous deformation, Acta Metall. 6 (11) (1958) 680–693.
[48] D.S. Lieberman, M. Wechsler, T. Read, Cubic to orthorhombic diffusionless phase change—experimental and theoretical studies of AuCd, J. Appl. Phys. 26 (4) (1955) 473–484.
[49] C.M. Wayman, Introduction to the crystallography of martensitic transformation, New York, Macmillan (1964).
[50] K. Otsuka, C.M. Wayman, Shape Memory Materials, Cambridge University Press, 1999.
[51] A. Acton, M. Bevis, A generalised martensite crystallography theory, Mater. Sci. Eng. 5 (1) (1969) 19–29.
[52] D. Dunne, G. Wayman, An assessment of the double shear theory as applied to ferrous martensitic transformations, Acta Metall. 19 (5) (1971) 425–438.

[53] A. Saldivar-Garcia, H. Lopez, Temperature effects on the lattice constants and crystal structure of a Co-27Cr-5Mo low-carbon alloy, Metall. Mater. Trans. A 35 (8) (2004) 2517–2523.
[54] X. Zhang, D. Li, Y. Li, S. Lu, Effect of aging treatment on the microstructures and mechanical properties evolution of 2Cr-20Ni austenitic stainless steel weldments with differnet Nb contents, J. Mater. Sci. Technol. 35 (2019) 520–529.
[55] J. Erneman, M. Schwind, P. Liu, J.O. Nilsson, H.O. Andren, J. Agren, Precipitation reactions caused by nitrogen uptake during service at high temperatures of a niobium stabilised austenitic stainless steel, Acta Mater. 52 (2004) 4337–4350.
[56] A. Zisman, Unique properties of habit plane (557) in origination of lath martensite, Mater. Lett. 275 (2020) 128140.
[57] E. Farabi, P.D. Hodgson, G.S. Rohrer, H. Beladi, Five-parameter intervariant boundary characterization of martensite in commercially pure titanium, Acta Mater. 154 (2018) 147–160.
[58] D.M. Saylor, A. Morawiec, G.S. Rohrer, Distribution and energies of grain boundaries in magnesia as a function of five degrees of freedom, Journal of the American Ceramic Society 85 (2002) 3081–3083.
[59] B. Hutchinson, J. Komenda, G.S. Rohrer, H. Beladi, Heat affected zone microstructures and their influence on toughness in two microalloyed HSLA steels, Acta Mater. 97 (2015) 380–391.
[60] A.B. Greninger, A.R. Troiano, Crystallography of austenite decomposition, Trans. AIME 140 (1940) 307–336.
[61] N. Ross, A. Crocker, A generalized theory of martensite crystallography and its application to transformations in steels, Acta Metall. 18 (4) (1970) 405–418.